SAND2015-7094J

Room temperature deformation mechanisms of alumina particles observed from *in situ* micro-compression and atomistic simulations

Pylin Sarobol, Michael Chandross, Jay D. Carroll, William M. Mook,

Daniel C. Bufford, Brad L. Boyce, Khalid Hattar, Paul G. Kotula, and Aaron C. Hall

Sandia National Laboratories, Albuquerque, New Mexico, USA

Abstract:

Aerosol deposition (AD) is a solid-state deposition technology that has been developed to fabricate ceramic coatings nominally at room temperature. Sub-micron ceramic particles accelerated by pressurized gas impact, deform, and consolidate on substrates under vacuum. Ceramic particle consolidation in AD coatings is highly dependent on particle deformation and bonding; these behaviors are not well understood. In this work, atomistic simulations and *in situ* micro-compressions in the scanning electron microscope and the transmission electron microscope (TEM) were utilized to investigate fundamental mechanisms responsible for plastic deformation/fracture of particles under applied compression. Results showed that highly defective micron-sized alumina particles, initially containing numerous dislocations or a grain boundary, exhibited no observable shape change before fracture/fragmentation. Simulations and experimental results indicated that particles containing a grain boundary only accommodate low strain energy per unit volume before crack nucleation and propagation. In contrast, nearly defect-free, sub-micron, single crystal alumina particles exhibited plastic deformation and fracture without fragmentation. Dislocation nucleation/motion, significant plastic deformation, and shape change were observed. Simulation and TEM *in situ* micro-compression results indicated that nearly defect-free particles accommodate high strain energy per unit volume associated with dislocation plasticity before fracture. The identified deformation mechanisms provide insight into feedstock design for AD.

1. Introduction

Aerosol deposition (AD) is a room temperature (RT) deposition process that can be used to fabricate ceramic coatings in solid-state. Sub-micron ceramic particles are accelerated to high velocity (200–600 m/s) by

pressurized gas at RT under low vacuum (Ref 1–10), and, the particles are impacted, deformed, and consolidated on a substrate. This technique enables high deposition rates (10–30 μm/min over a 1 cm^2 area), and can form thick films (~1–80 μm) with high integrity and properties equivalent to or exceeding conventionally prepared ceramics (Ref 4–6). Aerosol deposition of a variety of ceramics including structural (Al_2O_3, TiO_2, AlN) (Ref 1–3, 6, 11–16), dielectric ($BaTiO_3$) (Ref 4, 5), piezoelectric (PZT, PNN, $Bi_4Ti_3O_{12}$) (Ref 2, 3, 6–8, 17), magnetic (Sm-Fe-N) (Ref 9, 10), and battery ($LiMn_2O_4$, $LiCoO_2$) (Ref 5) materials has been reported. Normally, these materials are processed at temperatures above 800 °C, limiting integration with metals, plastics, or glasses. Room temperature ceramic deposition enables multi-materials fabrication and integration, although underlying mechanisms are not well understood. Understanding particle deformation and particle-particle bonding in the AD process requires knowledge of the fundamental deformation mechanisms in sub-micron ceramic particles.

Computational simulations have been used to gain insights into particle bonding mechanisms. Finite element modeling of 0.3–0.5 μm Al_2O_3 particles impacting an Al_2O_3 substrate at 300–400 m/s was performed by Akedo (Ref 3), Chun *et al*. (Ref 11), and Park, *et al*. (Ref 12). The common findings were that during impact, the particles experience high pressure and temperature rise at the particle/substrate interface while they plastically deform and fracture into small crystallites (20–75 nm). Additionally, Park *et al*. found that particles experience shock-induced amorphization (Ref 12), as has been reported elsewhere for ceramics in literature (Ref 18–20).

In the AD process, sub-micron particles undergo compression, plastic deformation, and fracture during impact with the substrate or the pre-deposited layer of coating. Although different in compression rate and geometry, *ex situ* and *in situ* compression experiments have been used to understand how ceramic particles deform in relevance to AD. Akedo and Ogiso (Ref 1) used modified tips in an atomic force microscope to compress 5.0 and 0.5 μm α-Al_2O_3 particles. They showed the 5.0 μm particles fractured, which would cause coating erosion, whereas 0.5 μm particles plastically deformed, which would facilitate coating consolidation. Consequently, sub-micron particle size is important for successful AD of ceramics. It also appears that some common mechanisms for particle deformation/bonding for different ceramics exist. In this work, RT deformation of individual sapphire (α-Al_2O_3) particles was examined computationally and experimentally as a model system for understanding the complex dynamics associated with *in vacuo* RT deposition conditions associated with AD.

Pre-existing defects of various types (e.g. mobile dislocations, stacking faults, twins, grain boundaries, cracks, etc.) lead to the diverse deformation behaviors observed in compressed materials with high degrees of ionic or covalent bonding, and are especially important with decreasing size (e.g. micro-pillars and particles) (Ref 21–28). Montagne *et al*. (Ref 21) performed RT micro-pillar compression experiments on different orientations of α-Al_2O_3 single crystals. The observed deformation behaviors of the pillars fit consistently into two categories—(1) pillars initially containing no defects exhibited consistent and *high* uniaxial stress at the load drop and visible slip planes or (2) pillars initially containing surface defects (induced by sample preparation via ion beam milling) exhibited inconsistent and *lower* uniaxial stress at the load drop and cracks. For ceramic particles, numbers of pre-existing defects are likely correlated with size, given that the distribution of defects is statistical. We hypothesized the following deformation mechanisms for differently sized ceramic particles in compression;

(1) in nanoscale (tens of nm diameter) ceramic particles (without pre-existing defects or dislocations), deformation is governed by plasticity, and can accommodate a higher strain energy (SE) per unit volume associated with dislocation nucleation and slip;

(2) in large (several micron diameter and above) ceramic particles (with many initial flaws and defects, including high numbers of immobile dislocations), deformation is governed by fracture, and can accommodate a lower SE per unit volume before crack initiation and propagation;

(3) in small (hundreds of nm diameter) particles, (with some initial immobile dislocations), a combination of fracture and plasticity governs deformation. This leads to more experimental scatter where particles can accommodate intermediate SE per unit volume before dislocation nucleation and slip preceding crack nucleation and propagation.

Here we use a combination of methods to elucidate the mechanisms responsible for the observed size-dependent deformation behavior in nano, sub-micron, and micron sized α-Al_2O_3 particles under compression. Atomistic simulations were used to test hypothesis (1), while *in situ* particle micro-compression in a scanning electron microscope (SEM) and in a transmission electron microscope (TEM) was used to test hypotheses (2) and (3).

2. Procedure

2.1 Atomistic Simulation

Molecular dynamics (MD) allows identification of dislocations, slip planes, and particle fracture. In this study, a force-field (FF) for ceramics developed by Garofalini (Ref 29) was used (Large-scale Atomic/Molecular Massively Parallel Simulator, LAMMPS). This FF accurately predicted surface structures, defect concentrations, and intergranular film composition in a variety of ceramics. Fracture surfaces have been studied with this FF (Ref 30), although fracture and plasticity have not. Computational limitations restricted our MD simulations to particle diameters < 50 nm (~36 million atoms). To circumvent this size limitation, we used the hypothesis that 'smaller' particles (< 1 μm) are nearly defect-free, and 'larger' particles (> 1 μm) contain initial immobile dislocations or a grain boundary (GB). We simulated two similarly sized 10 nm (~300,000 atoms) nanoparticles (NPs) that were either a single crystal or a bicrystal. We postulated that, in compression, the single crystal NP will accommodate higher SE and show dislocation plasticity, whereas the bicrystal NP, will accommodate lower SE and fracture. This approach enables us to study NP response to compression in computationally-feasible systems.

Spherical NPs were created from an initial bulk single crystal α-Al_2O_3 with the basal plane {0001} oriented perpendicular to the compression direction. The single crystal NP was created by removing all atoms that did not lie within a 5 nm prescribed radius from the NP center. The bicrystal NP was created by duplicating the single crystal NP and given a known rotation along the three Euler angles (Bunge convention). The initial and rotated NPs were both cut in half along the XZ-plane and joined at the center. The NPs were energy minimized at 0 K, followed by equilibration at RT for 1 ns. Both the single crystal and bicrystal NPs were compressed between two single crystal α-Al_2O_3 walls at a constant velocity of 20 m/s. Particles were compressed by ~1/3 of the initial particle diameter, and potential energy, force, and stress as a function of separation were calculated.

2.2 Particle Characterization and Compression

High purity α-Al_2O_3 particles with nominal sizes of 3 μm and 0.3 μm were obtained from Sumitomo Chemical Co., LTD. The electron transparent 0.3 μm Al_2O_3 particles were dispersed directly onto a carbon-coated copper TEM grid. The 3 μm particles were cross-sectioned using the focused ion beam (FIB) and prepared for subsequent *in situ* lift-out for TEM imaging. Microscopy was performed on both sets of the particles with an FEI

Tecnai F30-ST TEM/STEM operated at 300 kV. A combination of bright and dark-field TEM/STEM and selected area diffraction were used to investigate defects in the particles.

Micro-compression in the SEM was performed on both the 3 μm and 0.3 μm particles. The particles were suspended in ethanol and drop cast onto {0001} sapphire substrates. The compression axis was perpendicular to the {0001} sapphire substrate surface whereas the imaging axis was at 86° relative to the compression axis so that the indentation process could be observed *in situ*. The Zeiss Supra 55VP field emission gun SEM was operated at 5.0 kV. All particle loading was performed using a Hysitron PI85 SEM Picoindenter (Ref 31) in displacement control mode. A 3 μm diameter boron-doped diamond flat punch tip at a nominal 15 nm/s was used to compress the 0.3 μm particles, whereas a 6 μm diameter flat punch tip at a nominal 150 nm/s was used to compress the 3 μm particles (see Table 1 for actual values)[1]. Compression rate (calculated as the displacement rate divided by the initial particle diameter) of 0.05 s^{-1} and 0.005 s^{-1} were used for the small and large particles, respectively.

Micro-compression in the TEM was performed only on the electron transparent 0.3 μm particles. All TEM compression testing used an *in situ* Hysitron PI95 TEM Picoindenter with a 1 μm diameter boron-doped diamond flat punch tip, and was performed in a JEOL 2100 LaB_6 TEM (Ref 32) at 200 kV and imaged in bright-field mode. Compression was performed in open loop mode with a loading rate of 10 μN/s (corresponding to a displacement rate of ~2 nm/s and compression rates of ~0.007s^{-1}). Small particle response was observed *in situ.*

3. Results and Discussion

3.1 Molecular Dynamics Simulations

Fig. 1 and Fig. 2 show snap shots of atom positions on a thin slice though the simulated, spherical, 10 nm single crystal NP and the bicrystal NP during compression (see full videos in the supplemental files #1 and #2). Both NPs deformed plastically but did so differently. For the single crystal NP, primary dislocations (appeared as parallel lines in Fig. 1B) nucleated from the Al_2O_3 wall/NP contact points and moved through the NP (Fig. 1B) on rhombohedral planes $\{1\ \bar{1}\ 0\ 2\}$ (Fig. 1C). With further compression, secondary dislocations (appeared as parallel

[1] It is believed that the order of magnitude difference in compression rate is not large enough to introduce substantial effects. Experimental measurements from large particle #1 (LP1), subjected to the higher compression rate of 0.03 s^{-1} were in-line with values from other large particles.

lines oriented perpendicular to the primary dislocations in Fig. 1D), also nucleated from the Al_2O_3 wall/NP contact points, moved inward from the particle surface and terminating at the primary dislocations. Note that the rhombohedral plane was one of the reported common slip planes in Al_2O_3 (Ref 33–37). Finally, void nucleation occurred and the NP fractured[2] then separated into segments (Fig. 1E-F). For the bicrystal NP, at the Al_2O_3 wall/NP contact points, atoms from the left and right halves of the NP moved into the GB (Fig. 2B-C). With further compression, void nucleation occurred at the GB and the bicrystal NP fractured[2] (Fig. 2D-E). No dislocation nucleation or movement was observed in the bicrystal NP. After both NPs fractured, some areas in the NPs appeared crystalline with different orientations, while others appeared amorphized (Fig. 1F and Fig. 2E).

Force vs. compression distance was calculated for both NPs and shown in Fig. 3. For both NPs, force increased with increasing compression distance, reached a peak value, and then dropped. The large force drop for our simulated compressed single crystal NP appeared similar to those reported in micro-compression experiment, when the small compressed volume cracked. The peak force in the single crystal NP is substantially higher than that of the bicrystal NP, and the absorbed SE (calculated by integrating the force vs. displacement curve up to the peak value, marked 'X' in Fig. 3) is higher for the single crystal NP by a factor of 2.9. Calculated compression ratio (particle initial height divided by final height) prior to the force drop is also higher for the single crystal NP by a factor of 1.5. The high SE is associated with dislocation plasticity—mobile dislocation nucleation and movement—in the initially defect-free, single crystal NP. From this result, it is clear that mobile dislocations are needed to initiate plastic deformation prior to fracture. In contrast, an immobile defect—a GB—can act as a void nucleation site, providing no dislocation plasticity prior to particle fracture.

3.2 Pre-existing Defects in Particles

TEM observations confirmed that the as-received 3 μm particles contained many defects (Fig. 4). Fig. 4A shows a 3 μm particle that is relatively dislocation-free but contains a low-angle GB (lower part of grain) as an immobile defect. Fig. 4B shows a weak-beam dark field image of another 3 μm Al_2O_3 particle with numerous

[2] Here we use the term "fracture" in a general sense. It is unclear whether the observed event was truly fracture (i.e. no atomic bonds) as opposed to amorphization or crystallographic rotation in the center of the particles. Analysis showed the stress parallel to the compression axis at the center of both NPs decreased shortly after void nucleation, suggesting that subsequent fracture may have occurred and relieved the stress.

dislocations and stacking faults. In contrast, the 0.3 μm particles were largely defect-free but still contained some amount of pre-existing dislocations (Fig. 5). Numbers of dislocations vary from particle to particle. Fig. 5A shows a 0.3 μm particle that is relatively dislocation-free, whereas Fig. 5B shows two 0.3 μm alumina particles sharing a sintered GB with both grains containing dislocation loops (arrows). Pre-existing defects including dislocations in the particles were likely immobile and introduced during particle precipitation. We believe the presence of defects and numbers of dislocations highly influence particle responses during compression at these small length scales.

3.3 Particle Responses to Compressive Loading

Particle compression in the SEM revealed that the 3 μm "large" diameter particles, which contained higher numbers of pre-existing dislocations or GBs (recall Fig. 4), exhibited *brittle fracture and fragmentation* (Fig. 6A and Fig. 6B). Conversely, the 0.3 μm diameter "small" particles, which contained very few pre-existing dislocations (recall Fig. 5), exhibited a range of responses to compression, including significant *plastic deformation, shape change, orientation spread (mosaicity), and cracking without fragmentation* (Fig. 6C and Fig. 6F). Fig. 6F shows a 'flattened' particle that appeared similar to 'splats' typically seen in thermal or cold sprayed coatings. Coincidentally, this particle was accidentally loaded at a much higher compression rate (estimated near 4 s^{-1}) after it had been loaded quasistatically. The load vs displacement curves as well as images taken before and after compression for four large (3.0 μm) particles (designated as "LP's") are shown in Fig. 7 (See an example compression video in the supplemental file #3 for particle LP5) and those for four small (0.3 μm) particles (designated as "SM's") are shown in Fig. 8 (See an example compression video in the supplemental file #4 for particle SP5). For each particle, the load initially increased rapidly with increasing displacement. It was difficult to determine the exact transition from elastic regime to plastic regime. Initial load vs. displacement curves for large particles (Fig. 7) are nearly linear with smooth slopes; conversely, load vs. displacement for small particles (Fig. 8) appeared wavy with many small perturbations (i.e. pronounced displacement gain with low increase in load). These perturbations were not observed in the load vs. displacement curves for large particles, even when they were plotted on a similar scale. These small displacement bursts in compressed small particles suggested dislocation avalanches. At some critical load, both small and large particle load vs. displacement curves exhibited

a large displacement burst (i.e. a large displacement gain at a relatively constant load) when the particle fractured/collapsed[3]. Finally, the load dropped due to retraction of the tip as the control system recovered.

The particle size, compression rate, and corresponding volumetric strain energy density (VSED), areal strain energy density (ASED), as well as compression ratio at fracture, of all particles are summarized in Table 1. The apparent SE at fracture was estimated by integrating under the load vs. displacement curve up to the first fracture event (marked 'X' on all the curves in Fig. 7 and Fig. 8). Assuming that each particle is spherical, the VSED is calculated by normalizing the apparent SE at fracture by the particle volume. VSED at fracture represents the accommodated SED associated with dislocation activity throughout the volume. Assuming each particle experienced a through-particle fracture and that two new fracture surfaces were created, the ASED is calculated by normalizing the apparent SE at fracture with twice the particle cross-sectional area. ASED at fracture approximates the material's (i.e. Al_2O_3) resistance to fracture, similar to toughness. The two different SED's measure two distinct phenomena: VSED is a measure of plasticity, dislocation activity, and fracture, which consume energy throughout the material volume; on the other hand, ASED is a measure of fracture toughness because the fracture process involves transferring energy into new fracture surfaces. Finally, the compression ratio at fracture was calculated by normalizing the total displacement with the initial particle diameter.

The VSED at fracture varied due to different amounts of pre-existing (and likely immobile) dislocations or other defects in the particles and different loading orientations. The average VSED at fracture for the small particles was 630 ± 238 MJ/m^3 – six times higher than that for the large particle average, 106 ± 69 MJ/m^3. It is hypothesized that the higher VSED was associated with dislocation nucleation/movement in the small particles, as predicted by simulation and evidenced by waviness of the load vs. displacement curve in Fig. 8. The significantly higher VSED measured in small particles indicates they can accumulate more plasticity before fracture.

The ASED at fracture was found to be relatively independent of particle size. The ASED values reported in Table 1 (28–196 J/m^2 or 35–92 J/m^2 excluding two outliers) are near the calculated range of orientation-dependent crystal strain energy release rate (i.e. a value indicating the 'toughness') of single crystal alumina,

[3] The displacement bursts with apparent constant loads are a result of the control system failing to keep up with the rapidly collapsing particle, although these SEM micro-compression tests were performed in displacement control mode.

which is 16 J/m^2 to 65 J/m^2 (Ref 38). As shown in Fig. 6 and Fig. 7, there are multiple fractures for the large particles. If these fractures occurred simultaneously, the resulting ASED values would be even lower than reported in Table 1 and closer to the small particle values and the reported values (Ref 38). The close agreement in ASED for small and large particles indicates that it is a materials property that is relatively size-independent. It also suggests that the electron beam induced plasticity phenomenon likely did not occur during our micro-compression experiments.

The average compression ratio at fracture of small particles was 18 ± 9%, over twice that of the large particles, 5.5 ± 1%. Fast fracture/fragmentation of the 3 μm large particles was observed *in situ* during compression in the SEM. Similarly-sized particles were reported *not* to consolidate in AD process (Ref 1), suggesting a lack of particle plasticity and bonding. The kinetic energy density for small and large particles traveling at 200-600 m/s during AD process is estimated to be 79-711 MJ/m^3. Assuming very little kinetic energy is converted to heat, as most kinetic energy is converted to SE absorbed during impact, we suspect that large particles traveling at >233 m/s would fracture. In contrast, small particles traveling at <565 m/s would accommodate high enough SE associated with dislocation plasticity (without fracture), providing consolidation. Accordingly, one would hypothesize that small particles traveling at >565 m/s would fracture during impact, likely resulting in poor coating consolidation.

Detailed examination of small (0.3 μm) particles under compression in the TEM showed that pre-existing dislocations appeared immobile and did not participate in the plastic deformation process. Instead, nucleated dislocations that are *mobile* and present in high quantity contribute to the observed particle significant plasticity and shape change. Thus both simulation and experiments verified that high VSED's were associated with dislocation nucleation/movement to initiate plastic deformation and shape change. An example is demonstrated in Fig. 9 and video in the supplemental file #5. Compression of a near defect-free, single crystal particle showed parallel dislocations rapidly nucleated from the tip/particle interface and moved through the particle, followed by a through-particle fracture. Parallel dislocation lines observed in compression experiment was remarkably similar to those observed in the simulated compressed single crystal NP. Another compressed particle (TEM-SP1)

showed similar parallel dislocations with the addition of orientation spread, where the particle separated into many small crystallites. Diffraction patterns, collected from the deformed TEM-SP1 particle after compression, showed orientations of the small crystallites span over a 20 degree rotation from its initial single crystal grain orientation. Note, AD ceramic films in literature, including Al_2O_3, $BaTiO_3$, and PZT, appear to possess similar microstructural characteristics, where deformed particles contain small (20-75 nm) crystallites (Ref 5). In this work, amorphous regions were not observed in the experimentally deformed particles due to low compression rate. We believe our compression rate and relatively low energy density input during micro-compression were not sufficient to trigger the shock-induced amorphization observed in AD ceramic coatings (high strain rate and impact energy) by Park, *et al*. (Ref 12). Nonetheless, we have sufficient evidence from this work that mobile dislocations provide plasticity in small particles and play a key role in their deformation. Pre-straining the small particles by ball milling would introduce mobile dislocations. These pre-strained particles would only need to accommodate additional low VSED, i.e. travel at lower velocity, to plastically deform and consolidate. This may explain why literature reported ball-milling could improve deposition efficiency during AD process (Ref 8).

3.4 Deformation Mechanisms of Single Crystal Alpha-Alumina Particles under Compression

It is important to note several major differences between simulation and experiments. Simulations were performed at a high displacement rate of 20 m/s on very small (10 nm) Al_2O_3 NPs (compression rate ~ 2×10^9 s^{-1}). In contrast, experimental *in situ* micro-compression in the SEM and the TEM were performed on realistic 3 μm and 0.3 μm, Al_2O_3 particles at much lower displacement rates (~nm/s). Despite these differences, simulation and experimental results supported the proposed deformation mechanisms for compressed differently sized ceramic particles and suggested deformable sub-micron particles are building blocks of AD ceramic films.

Both the simulation and micro-compression results agree qualitatively. They show that compressed initially, relatively defect-free ('small') particles undergo significant plastic deformation/shape change prior to fracture whereas highly defective ('large') particles undergo fast fracture and fragmentation. Experiments showed the average compression ratio before fracture of the small particles was 3 times that of the large particles. Similarly, simulation showed the compression ratio before fracture of the defect-free single crystal NP was 1.5 times that of the bicrystal NP. Additionally, both results show that higher VSED are associated with dislocation

nucleation/motion (plastic deformation) of small ceramic particles that were initially relatively defect-free. In contrast, particles with an initial GB as an immobile defect built up less VSED before fracture. Specifically, experimental results showed the average VSED before fracture for the small particles was 6 times that of the large particles. Likewise, simulation results showed the average absorbed energy prior to fracture for the defect-free NP was 3 times that of the bicrystal NP. Moreover, both the simulation and *in situ* TEM micro-compression results showed dislocation nucleation/motion and separation into small crystallites. The VSED ratio of 6, between small and large particles, from experiments (rather than 2.9 from simulations) is likely due to displacement rate effect (nm/s vs. m/s) and having a single defect in bicrystal simulations as opposed to multiple defects in the experimental large particles. Presence of stress concentrators (facets/cracks) also contributed to the compression ratio being much smaller in the experiment particles than in the perfectly spherical simulated NPs.

Several implications in regards to AD emerged from this work. First, plastic deformation, shape change, orientation spread (mosaicity), and fracture without fragmentation are possible in sub-micron sized ceramic particles. These mechanisms contribute to coating buildup in AD. Sub-micron sized ceramic particles are capable of RT plastic deformation at low compression rate (as shown in this work) and high compression rate reported in the literature (Ref 5). Second, the use of sub-micron sized particles that contain pre-existing *mobile* dislocations (as opposed to dislocation-free particles or particles with *immobile* dislocations) will accommodate additional low VSED (corresponding to lower particle velocity in AD) with further deformation and will likely lead to higher deposition efficiency in AD. This is due to a lower VSED associated with moving the pre-existing *mobile* dislocations (as opposed to nucleating new dislocations) during the plastic deformation process. Pre-existing mobile dislocations could be introduced into particles via feedstock ball milling. Future work that further explores the effects of particle size, presence of mobile dislocations, crystal orientation, and strain rate on the observed particle deformation behavior, would provide valuable insights. Third, particles even smaller than 0.3 μm would be expected to also be relatively defect-free and able to deform plastically; however, their smaller size would mean lower impact energy in AD (due to lower mass). Consequently, AD of ceramics involves a compromise between plastic deformation, particle size, and impact energy.

4. Summary

Pre-existing defects play an important role in the deformation behavior of nano-, sub-micron, and micron sized alumina particles in compression. Atomistic simulations of defect-free alumina nanoparticles showed that nucleation/movement of mobile dislocations occured during compression and was accompanied by significant plastic deformation. This finding supports the idea of plasticity-governed deformation, in which nucleation/glide of dislocations control deformation of small particles. Simulated compression of a nanoparticle with an internal boundary as a pre-existing immobile defect did *not* result in dislocation plasticity. The findings from atomistic simulations are in good qualitative agreement with those from *in situ* micro-compression experiments. Relatively defect-free sub-micron alumina particles can accommodate high volumetric strain energy density associated with dislocation nucleation/motion (significant plastic deformation and shape change) when loaded in compression. These particles fractured but did not fragment. Micron-sized alumina particles, typically with large numbers of defects or a grain boundary only accommodated low volumetric strain energy density before fracture and fragmentation when loaded in compression. Implication from this work gave insights into particle size selection for aerosol deposition and mechanisms behind ball-milling to increase efficiency of room temperature consolidation in aerosol deposited ceramic films.

Acknowledgments

B.L. Boyce, K. Hattar, and D.C. Bufford were supported by the Department of Energy (DOE) office of Basic Energy Sciences, Materials Science and Engineering. The authors acknowledge Sumitomo Chemical Co., LTD for supplying the alumina particles. We are grateful to C.B. Carter, P. Clem, D. Hirschfeld, H. Brown-Shaklee, R.D. Murphy, R. Tandon, and E.D. Reedy for valuable discussions. This work was performed, in part, at the Center for Integrated Nanotechnologies (CINT), an Office of Science User Facility operated for the U.S. DOE Office of Science. This work is supported by the Laboratory Directed Research and Development program at Sandia National Laboratories, a multi-program laboratory managed and operated by Sandia Corporation, a wholly owned subsidiary of Lockheed Martin Corporation, for the U.S. DOE's National Nuclear Security Administration under contract DE-AC04-94AL85000.

Figures

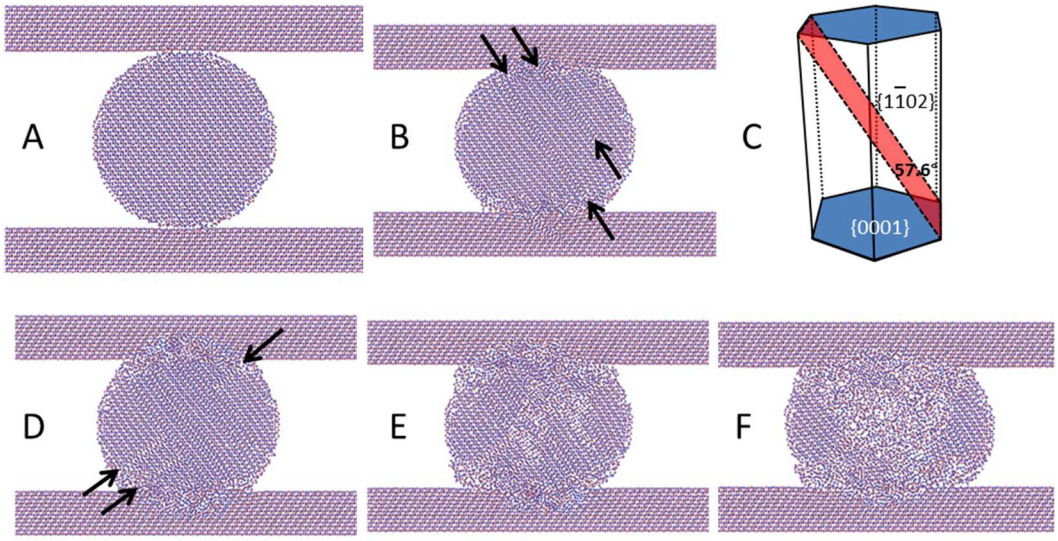

Fig. 1 Thin slices through a 10 nm single crystal NP with {0001} plane perpendicular to the compression direction, showing atom positions at different stages of compression. The single crystal alumina walls were moved towards each other at a speed of 20 m/s. (a) moment at first contact. (b) moment after the primary parallel dislocations nucleated at the top contact plane and moved through the particle (arrowed). (c) The 57.6° between slip planes and basal planes suggested that slip planes were rhombohedral, $\{1\ \bar{1}\ 0\ 2\}$. (d) Secondary dislocations nucleated (arrowed) and moved from the particle surface inward, terminating at the primary dislocations. (e) Void nucleation. (f) Particle fracture and separation. See video in the supplemental file #1 for a full compression.

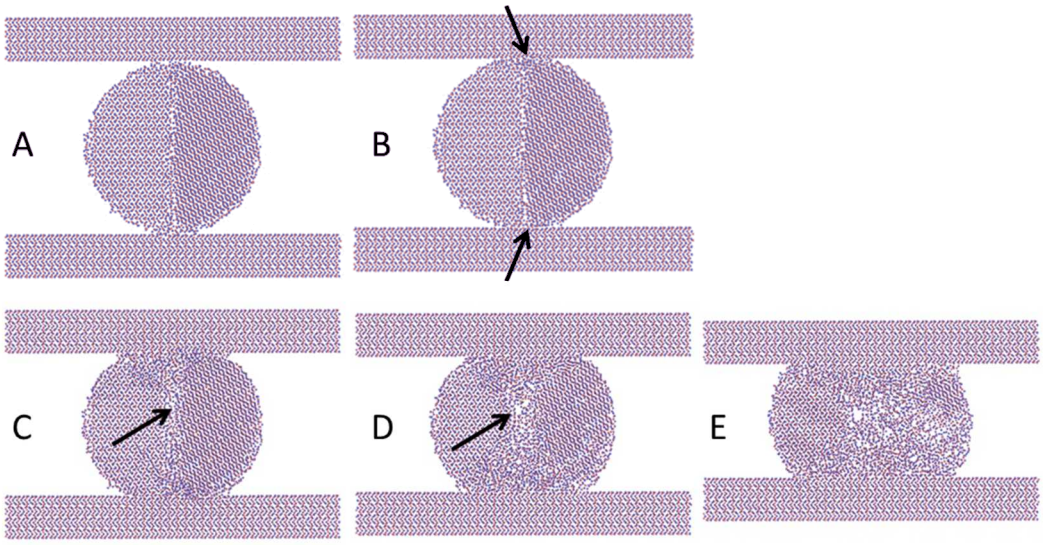

Fig. 2 Thin slices through a 10 nm bicrystal NP, showing atom positions at different stages of compression. The left side of the bicrystal NP has the {0001} plane perpendicular to the to the compression direction. The right side of the bicrystal NP is randomly rotated. (a) Moment at first contact; (b) Atoms from the particle surface at the contact points moved down the grain boundary (arrowed); (c) Moment before void nucleation; (d) Void nucleation at the grain boundary (arrowed); (e) Particle fracture and separation. See video in the supplemental file #2 for a full compression.

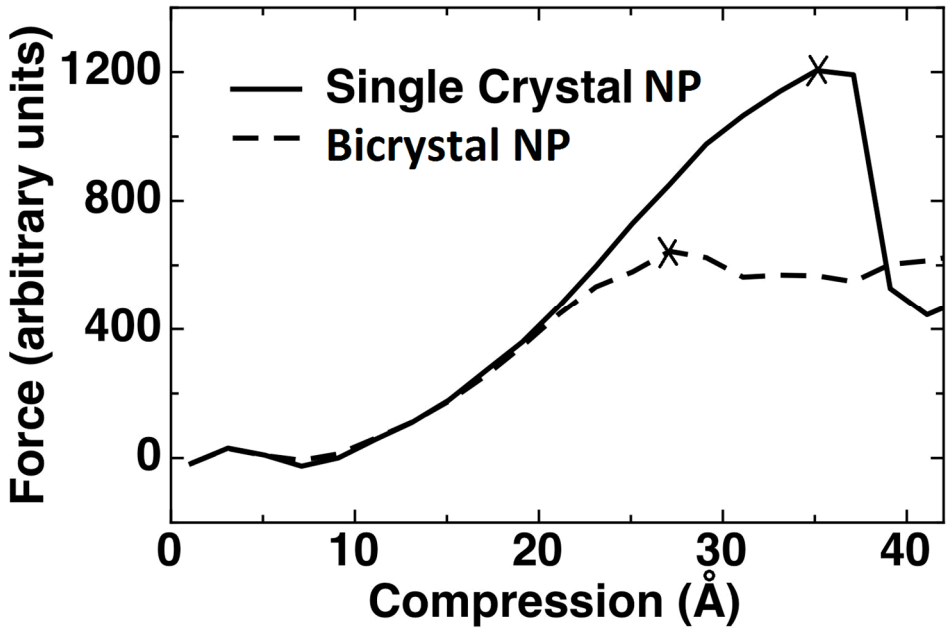

Fig. 3 Force vs. displacement (Angstrom) for the 10 nm diameter NPs—a single crystalline NP with no defects (solid curve) and the bicrystal NP with a grain boundary as an immobile defect (dashed curve). The "X" on each curve marks the fracture point.

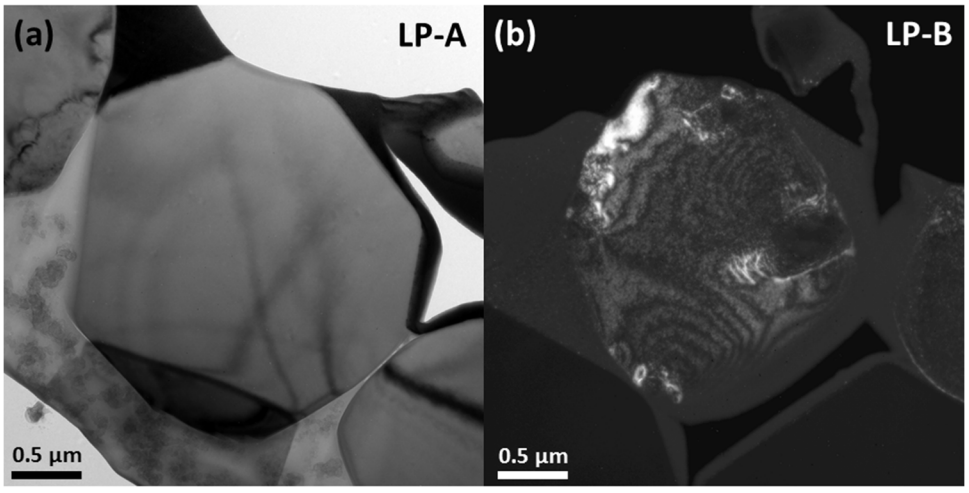

Fig. 4 (a) bright-field TEM image from a largely dislocation-free as-received 3 µm particle, LP-A, containing a low angle grain boundary as an immobile defect. Note the grain boundary separated the light region and the dark region in the lower part of the particle; (b) a weak-beam dark-field TEM image of a different 3 µm particle, LP-B, that is single-crystalline but contains many dislocations and stacking faults.

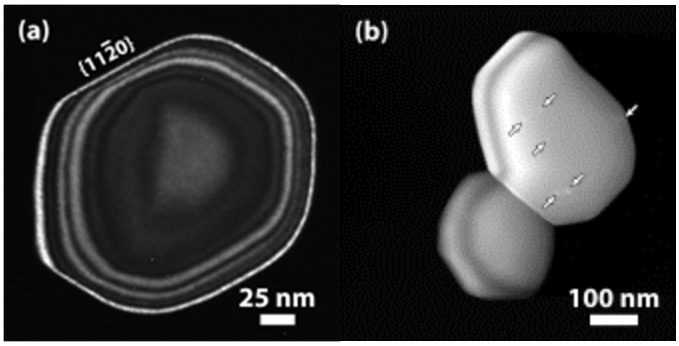

Fig. 5 Images showing the 0.3 μm Al_2O_3 particles. All particles were relatively defect-free. (a) Dark field TEM image of a faceted particle in a diffracting condition (looking down the basal plane normal). (b) Dark field STEM image of two alumina particles sintered together. The arrows point to dislocations.

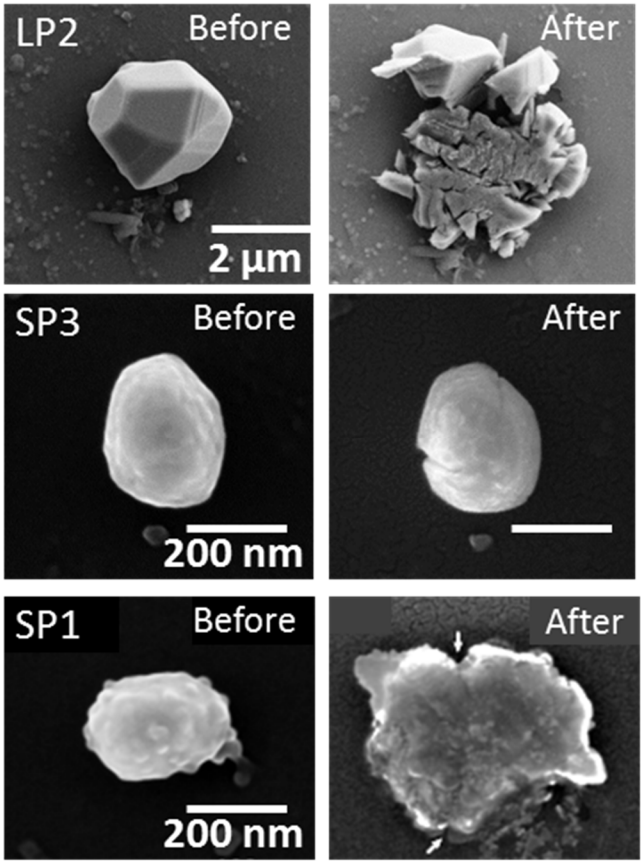

Fig. 6 SEM images before and after compression of 3 μm and 0.3 μm alumina particles. The 3 μm particle, LP2, fragmented into many pieces upon compression. The small 0.3 μm particle, SP3, cracked in compression, but stayed mostly intact; this particle also appeared to change shape slightly. The small 0.3 μm particle, SP1, was loaded with a high force at high compression rate, resulting in substantial plasticity and little apparent fragmentation despite an apparent crack indicated by arrows.

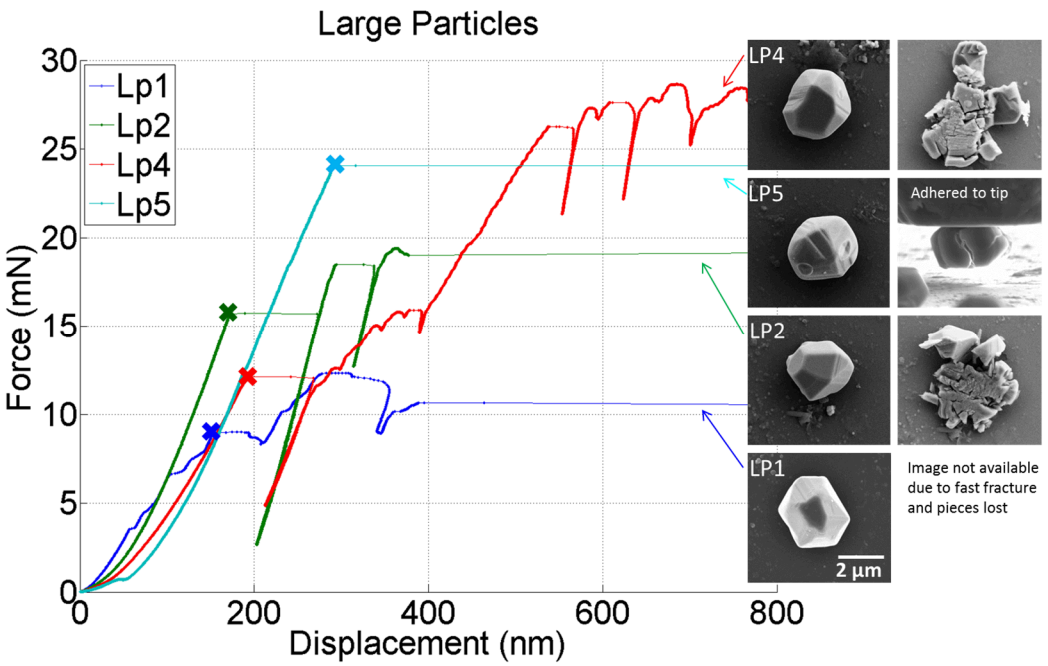

Fig. 7 Load vs. displacement curves using a Hysitron PI85 SEM Picoindenter in the displacement control mode as well as SEM images before and after loading for four 3 µm particles (LP1, LP2, LP4, and LP5). The "X" on each curve marks the first fracture event for each particle. See an example compression video in the supplemental file #3 for particle LP5.

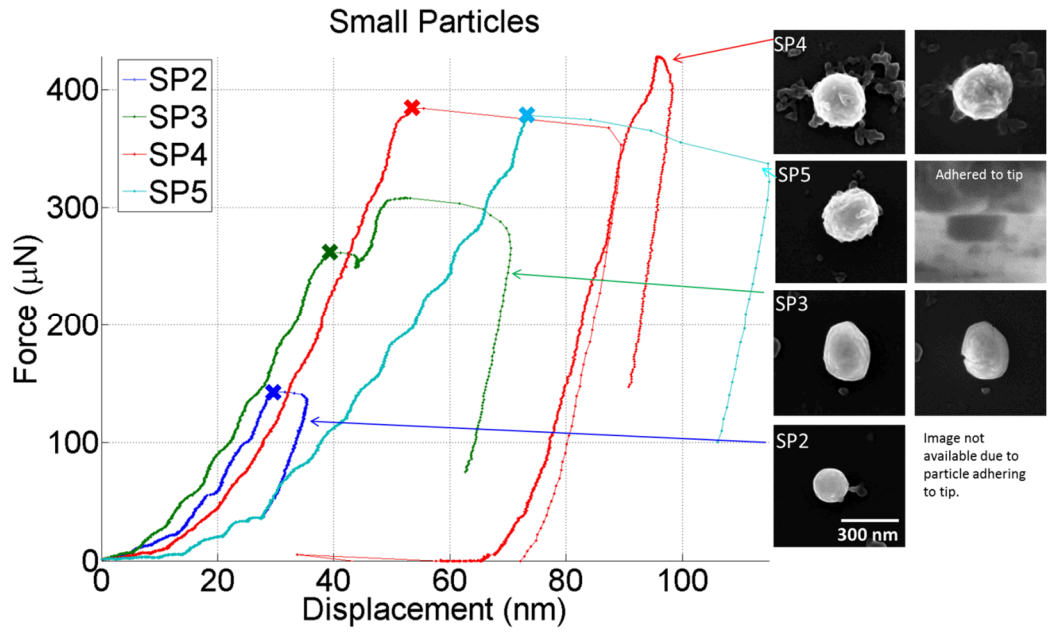

Fig. 8 Load vs. displacement curves using a Hysitron PI85 SEM Picoindenter in the displacement control mode and SEM images before and after loading for four 0.3 µm particles (SP2-SP5). Waviness in the curve is associated with dislocation avalanche. The "X" on each curve marks the first fracture event for each particle. See an example compression video in the supplemental file #4 for particle SP5.

Table 1 Diameter, compression rate, as well as corresponding VSED, ASED, and compression ratio at fracture for all particles compressed in the SEM and the TEM.

Particle Identifier	Diameter (µm)	Compression Rate (s^{-1})	Volumetric Strain Energy Density (VSED) at fracture (MJ/m^3)	Areal Strain Energy Density (ASED) at fracture (J/m^2)	Compression Ratio before fracture (%)
Large Particles					
SEM-LP1	2.9	0.03	47	45	5
SEM-LP2	2.6	0.006	106	92	5
SEM-LP4	2.9	0.005	70	67	5
SEM-LP5	2.9	0.003	203	196	7
Avg Large Particles	**2.8**	**-**	**106±69**	**100±67**	**5.5 ± 1**
Small Particles					
SEM-SP2	0.17	0.09	494	28	11
SEM-SP3	0.29	0.05	366	35	12
SEM-SP4	0.28	0.05	607	57	13
SEM-SP5	0.29	0.05	675	65	16
TEM-SP2	0.38	0.005	573	73	32
TEM-SP1	0.24	0.009	1066	83	27
Avg Small Particles	**0.26**	**-**	**630±238**	**57±21**	**18 ± 9**

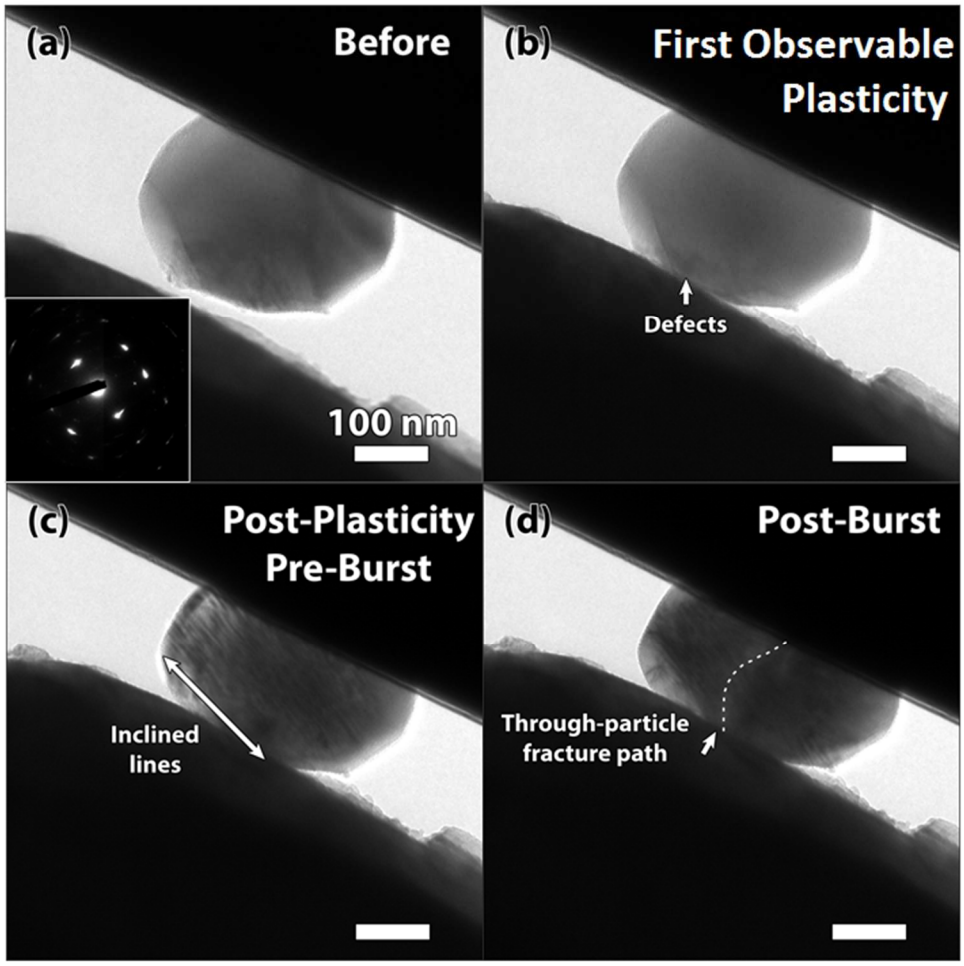

Fig. 9 TEM images and an initial diffraction pattern on a 0.3 μm diameter alumina particle during compression using the Hysitron PI95 TEM Picoindenter in open loop mode in the TEM. (a) single crystal particle was relatively defect-free before compression; (b) first observable sign of plasticity was marked by parallel dislocation nucleation (arrowed) at the contact between the tip and the particle; (c) parallel dislocations (appeared as inclined lines) moved through the particle moments before displacement burst / particle fracture; (d) though-particle fracture occurred during the displacement burst. The fracture line may not be clear in image (d) but it is evident in the compression video in supplemental file #5.

References

1. J. Akedo and H. Ogiso, "Room Temperature Impact Consolidation (RTIC) of Ceramic Fine Powder on Aerosol Deposition," *Proc. of the 2nd International Conference and Exhibition on Ceramic Interconnect and Ceramic Microsystems Technologies, CICMT* 2006.
2. J. Akedo, "Room Temperature Impact Consolidation (RTIC) of Fine Ceramic Powder by Aerosol Deposition Method and Applications to Microdevices." *JTTEE5*, 2008, **17**, p. 181-198.
3. J. Akedo, "Aerosol Deposition of Ceramic Thick Films at Room Temperature Densification Mechanism of Ceramic Layers," *J. Am. Ceram. Soc.*, 2006, **89**, p. 1834-1839.
4. Y. Imanaka, N. Hayashi, M. Takenouchi, and J. Akedo, "Technology for Embedding Capacitors on Printed Wiring Board Using Aerosol Deposition," *Proc. of Ceramic Interconnect and Ceramic Microsystems Technologies*, (2006).
5. Y. Imanaka, N. Hayashi, M. Takenouchi, and J. Akedo, "Aerosol Deposition for Post-LTCC," *J. Euro. Ceram. Soc*. 2007, **27**, p. 2789-2795.
6. J. Akedo, "Aerosol Deposition Method for Fabrication of Nano Crystal Ceramic Layer – Novel ceramic coating with collision of fine powder at room temperature," *Materials Science Forum*, 2004, **449-452**, p. 43-48.
7. Y. Kawakami, H. Yoshikawa, K. Komagata, and J. Akedo, "Powder Preparation for $0.5Pb(Ni_{1/3}Nb_{2/3})O_3$-$0.15PbZrO_3$-$0.35PbTiO_3$ Thick Films by the Aerosol Deposition Method," *J. Crys. Growth.* 2005, **275**, p. el295-el300.
8. J. Akedo and M. Lebedev, "Piezoelectric Properties and Poling Effect of $Pb(Zr,Ti)O_3$ Thick Films Prepared for Microactuators by Aerosol Deposition," *Appl. Phys. Lett*. 2000, **77**, p. 1710-1712.
9. S. Sugimoto, T. Maeda, R. Kobayashi, J. Akedo, M. Lebedev, and K. Inomata, "Magnetic Properties of Sm-Fe-N Thick Film Magnets Prepared by the Aerosol Deposition Method," *IEEE Trans. Magnetics*. 2003, **39**, p. 2986-2988.
10. S. Sugimoto, T. Maki, T. Kagotani, J. Akedo, and K. Inomata, "Effect of Applied Field During Aerosol Deposition on the Anisotropy of Sm-Fe-N Thick Films," *J. Magn. Magn. Mater*. 2005, **290-291**, p. 1202-1205.
11. D.M. Chun and S.H. Ahn, " Deposition mechanism of dry sprayed ceramic particles at room temperature using a nano-particle deposition system," *Acta Mater*, 2011, **59**, p. 2693-2703.
12. H. Park, J. Kwon, I. Lee, and C. Lee, "Shock-induced plasticity and fragmentation phenomena during alumina deposition in the vacuum kinetic spraying process," *Scripta Mater*, 2015, **100**, p. 44-47.
13. M. Schubert, J. Exner, and R. Moos, "Influence of Carrier Gas Composition on the Stress of Al_2O_3 Coatings Prepared by Aerosol Deposition Method," *Materials*, 2014, **7**, p. 5633-5642.
14. D.W. Lee and S.M. Nam, "Factors affecting surface roughness of Al_2O_3 films deposited on Cu substrates by an aerosol deposition method," *J. Ceram. Process. Res*. 2010, **11**, p. 100-106.
15. S.H. Cho and Y.J. Yoon, "Multi-layer TiO_2 films prepared by aerosol deposition method for dye-sensitized solar cells," *Thin Solid Films*, 2013, **547**, p.91-94.
16. Y.J. Heo H.T. Kim, K.J. Kim, S. Nahm, Y.J. Yoon, and J. Kim, "Enhanced heat transfer by room temperature deposition of AlN film on aluminum for a light emitting diode package," *Appl. Therm. Eng*. 2013, **50**, p. 799-804.
17. J. Exner, P. Fuierer, and R. Moos, "Aerosol Codeposition of Ceramics: Mixtures of Bi_2O_3-TiO_2 and Bi_2O_3-V_2O_5," *J. Am. Ceram. Soc*. 2015, **98**, p.717-723.
18. V. Swamy, A. Kuznetsov, L.S. Dubrovinsky, P.F. McMillan, V.B. Prakapenka, G. Shen, and B.C. Muddle, "Size-Dependent Pressure-Induced Amorphization in Nanoscale TiO_2," *Phys. Rev. Lett*. Vol. 2006, **96**, p. 135702-4.
19. M. Chen, J.W. McCauley, and K.J. Hemker, "Shock-Induced Localized Amorphization in Boron Carbide," *Science*, 2003, **299**, p. 1563-1566.
20. G. Subhash, S. Maiti, P.H. Geubelle, and D. Ghosh, "Recent Advances in Dynamic Indentation Fracture, Impact Damage and Fragmentation of Ceramics," *J. Am. Ceram. Soc*. 2008, **91**, p. 2777-2791.
21. A. Montagne, S. Pathak, X. Maeder, and J. Michler, "Plasticity and Fracture of Sapphire at Room Temperature: Load-Controlled Microcompression of Four Different Orientations," *Ceram Int*. 2014, **40**, p. 2083-2090.
22. A.R. Beaber, J.D. Nowak, O. Ugurlu, W.M. Mook, S.L. Girshick, R. Ballarini, and W.W. Gerberich, "Smaller is Tougher," *Philos. Mag*., 2011, **91**, p. 1179-1189.
23. W.W. Gerberich, J. Michler, W.M. Mook, R. Ghisleni, F. Ostlund, D.D. Stauffer, and R. Ballarini, "Scale Effects for Strength, Ductility, and Toughness in "Brittle" Materials," *J. Mater. Res.*, 2009, **24**, p. 898-906.
24. W.W. Gerberich, W.M. Mook, M.J. Cordill, C.B. Carter, C.R. Perrey, J.V. Heberlein, and S.L. Girshick, "Reverse Plasticity in Single Crystal Silicon Nanospheres," *Int J Plasticity*., 2005, **21**, p. 2391-2405.
25. F. Ostlund, K. Rzepiejewska-Malyska, K. Leifer, L.M. Hale, Y. Tang, R. Ballarini, W.W. Gerberich, and J. Michler, "Brittle-to-Ductile Transition in Uniaxial Compression of Silicon Pillars at Room Temperature," *Adv. Funct. Mater*., 2009, **19**, p. 2439-2444.

26. G. Xu and C. Zhang, "Analysis of Dislocation Nucleation from a Crystal Surface Based on the Peierls-Nabarro Dislocation Model," *J. Mech. Phys. Solids*, 2003, **51**, p. 1371-1394.
27. P.R. Howie, S. Korte, and W.J. Clegg, "Fracture Modes in Micropillar Compression of Brittle Crystals," *J. Mater. Res.*, 2012, **27**, p. 141-151.
28. F. Ostlund, P.R. Howie, R. Ghisleni, S. Korte, K. Leifer, W.J. Clegg, and J. Michler, "Ductile-Brittle Transition in Micropillar Compression of GaAs at Room Temperature," *Philos. Mag*. 2011, **91**, p. 1190-1199.
29. S. Blonski and S.H. Garofalini, "Molecular Dynamics Study of Silica-Alumina Interfaces," *J. Phys. Chem*., 1996, **100**, p. 2201-2205.
30. D.A. Litton and S.H. Garofalini, "Modeling of Hydrophilic Wafer Bonding by Molecular Dynamics Simulations," *J. Appl. Phys*., 2001, **89**, p. 6013-6023.
31. Hysitron I (2013) *SEM Picoindenter User Manual*. Revision 9.3.0913 edn.
32. K. Hattar, D.C. Bufford, and D.L. Buller, "Concurrent in Situ Ion Irradiation Transmission Electron Microscope," *Nuclear Instruments and Methods in Physics Research B*. 2014, **338**, p. 56–65.
33. N.I. Tymiak and W.W. Gerberich, "Initial stages of contact-induced plasticity in sapphire. I. Surfaces traces of slip and twinning," *Phil. Mag*., 2007, **87**, p. 5143-5168.
34. N.I. Tymiak and W.W. Gerberich, "Initial stages of contact-induced plasticity in sapphire. II. Mechanisms of plasticity initiation," *Phil. Mag*., 2007, **87**, p. 5169-5188.
35. R. Nowak, T. Sekino, and K. Niihara, "Surface deformation of sapphire crystal," *Phil. Mag. A*, 1996, **74**, p. 171-194.
36. J.D. Clayton, "A continuum description of nonlinear elasticity, slip and twinning, with application to sapphire," *Proc. Of the Royal Soc. A.,* 2009, **465**, p. 307-344.
37. E.R. Dobrovinskaya, L.A. Lytvynov, and V. Pishchik, "Properties of Sapphire," *Sapphire*, Springer, Boston, MA, US, 2009.
38. *Materials Science and Engineering Serving Society* edited by R.P.H. Chang, R. Roy, M. Doyama, and S. Somiya. (Elsevier Science, The Netherlands, 1998).